A Billion-fold Range in Acidity for the Solvent-Exposed Amides of *Pyrococcus furiosus* Rubredoxin

Janet S. Anderson,[‡] Griselda Hernández,[§] and David M. LeMaster*[,§]

Department of Chemistry, Union College, Schenectady, New York 12308, and Wadsworth Center, New York State Department of Health, and Department of Biomedical Sciences, School of Public Health, University at Albany-State University of New York, Empire State Plaza, Albany, New York 12201

Received February 18, 2008; Revised Manuscript Received April 16, 2008

ABSTRACT: The exchange rates of the static solvent-accessible amide hydrogens of *Pyrococcus furiosus* rubredoxin range from near the diffusion-limited rate to a billion-fold slower for the non-hydrogen-bonded Val 38 (eubacterial numbering). Hydrogen exchange directly monitors the kinetic acidity of the peptide nitrogen. Electrostatic solvation free energies were calculated by Poisson−Boltzmann methods for the individual peptide anions that form during the hydroxide-catalyzed exchange reaction to examine how well the predicted thermodynamic acidities match the experimentally determined kinetic acidities. With the exception of the Ile 12 amide, the differential exchange rate constant for each solvent-exposed amide proton that is not hydrogen bonded to a backbone carbonyl can be predicted within a factor of 6 ($10^{0.78}$) root-mean-square deviation (rmsd) using the CHARMM22 electrostatic parameter set and an internal dielectric value of 3. Under equivalent conditions, the PARSE parameter set yields a larger rmsd value of 1.28 pH units, while the AMBER parm99 parameter set resulted in a considerably poorer correlation. Either increasing the internal dielectric value to 4 or reducing it to a value of 2 significantly degrades the quality of the prediction. Assigning the excess charge of the peptide anion equally between the peptide nitrogen and the carbonyl oxygen also reduces the correlation to the experimental data. These continuum electrostatic calculations were further analyzed to characterize the specific structural elements that appear to be responsible for the wide range of peptide acidities observed for these solvent-exposed amides. The striking heterogeneity in the potential at sites along the protein−solvent interface should prove germane to the ongoing challenge of quantifying the contribution that electrostatic interactions make to the catalytic acceleration achieved by enzymes.

Exchange rates for the most slowly exchanging amide protons along the peptide backbone are widely used to estimate the global thermodynamic stability of a protein when direct calorimetric or spectroscopic measurements are impractical. In this analysis of protein stability, it is assumed that amides in the unfolded state exchange with the solvent at rates equivalent to rates for model peptides that possess the corresponding local sequence. When the commonly observed EX2 kinetic conditions apply, the ratio of the observed exchange rate for the most slowly exchanging amides to that of a model peptide under the same solution conditions would then correspond to the equilibrium constant for the unfolding transition. Although exceptions have been noted, the most slowly exchanging amides often appear to yield a reasonable estimate of thermodynamic stability (*1*).

On the other hand, under physiological conditions, the amides that exchange via a global unfolding transition generally constitute only a small fraction of the peptide backbone. A survey of 20 well-studied proteins identified less than 10% of all backbone amides as such "core" amides (*2*). By definition, the large majority of amides that do not exchange via a global unfolding transition retain residual conformational structure during their exchange. Interpretation of the rates for amides that do not exchange via a global unfolding mechanism has been commonly addressed by simply defining residue-specific conformational stabilities (*3*), which assumes that the hydrogen exchange rates for such amides are insensitive to the residual structure that is present in the exchange-competent conformation.

Static solvent-accessible amide protons (*5*) that lack intramolecular hydrogen bonds offer the most direct test of whether every amide in an exchange-competent conformation exhibits the same reactivity to exchange. A particularly interesting example of such an amide is Val 38 (eubacterial numbering) in the rubredoxin from the hyperthermophilic archaeon *Pyrococcus furiosus*, the most thermostable monomeric protein known to undergo reversible unfolding (*6*). Englander and co-workers (*7*) reported a residue-specific conformational stability of 7 kcal/mol for the Val 38 amide of *Pf* rubredoxin at 60 °C, yet as illustrated in the 0.95 Å resolution X-ray structure of this protein (*4*), the amide proton of Val 38 is highly exposed to the bulk solvent phase (Figure 1). No hydrogen bond acceptor is available unless a substantial change in the backbone conformation occurs, while the highly solvated Asp 36 is the nearest formal charge

* To whom correspondence should be addressed. E-mail: lemaster@wadsworth.org. Telephone: (518) 474-6396. Fax: (518) 473-2900.
[‡] Union College.
[§] New York State Department of Health and University at Albany-State University of New York.

10.1021/bi800284y CCC: $40.75 © 2008 American Chemical Society
Published on Web 05/15/2008

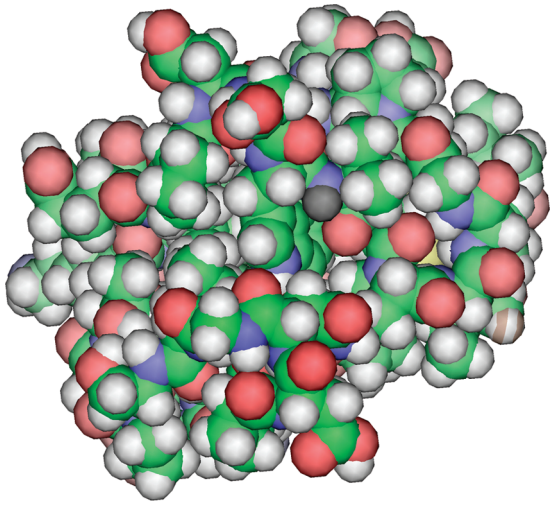

FIGURE 1: CPK representation of *Pf* rubredoxin. Coordinates were taken from the 0.95 Å resolution X-ray structure [Protein Data Bank (PDB) entry 1BRF (*4*)]. The amide proton of solvent-exposed Val 38 is indicated in black near the center of the figure.

(7 Å). Note that other proteins, such as phage T4 lysozyme (*8*), also have amides with reported exchange rates that are approximately a million-fold slower than reference peptide values, yet these amide protons are accessible to solvent in the corresponding X-ray structures. To gain further insight into such exchange behavior, we have determined the hydroxide-catalyzed rate constants for every amide proton that is solvent-exposed in the *Pf* rubredoxin X-ray structure.

EXPERIMENTAL PROCEDURES

Protein Sample Preparation. Construction of the gene for the A2K variant of *Pf* rubredoxin has been described previously (*9*). Protein expression was carried out in the BL21(DE3) system (Novagen) with a second plasmid that constitutively overproduces the methionine peptide deformylase to yield homogeneous N-terminal processing (*9*). Zn^{2+}-coordinated U-^{2}H- and U-^{15}N-labeled *Pf* A2K rubredoxin was expressed and purified as previously described (*10*). Aliquots of the protein were exchanged into a series of buffers, via centrifugal ultrafiltration, to a final protein concentration of 3 mM. Phosphate (for pH values of 6.00, 7.00, 7.94, and 11.85), borate (for pH values of 8.95 and 9.82), acetate (for a pH value of 4.93), and carbonate (for a pH value of 10.77) buffers at 20 mM in 6% $^{2}H_2O$ were adjusted to a total ionic strength of 150 mM with sodium chloride.

Nuclear Magnetic Resonance (NMR) Data Collection. Clean chemical exchange-phase modulated (CLEANEX-PM) (*11*) spectra with relaxation compensation (*12*) were collected on a Bruker Avance 500 MHz spectrometer at 25 °C with mixing times of 7.14, 14.27, 21.41, 28.55, and 35.58 ms as previously described (*13*). The intensity of each fully relaxed spectrum was estimated by exponential extrapolation of the intensities from the hard pulse reference experiment using relaxation delays of 2.0, 4.0, and 8.0 s.

Electrostatic Calculations. Hydrogen atoms were added to the X-ray coordinates of *Pf* rubredoxin [PDB entry 1BQ8 (*4*)] with Reduce (*14*). This rubredoxin variant contains an N-terminal Met-Ala sequence, while the sample used in our NMR analysis contains an N-terminal Met-Lys sequence. Nonlinear Poisson−Boltzmann calculations were carried out using the DelPhi algorithm (*15*). CHARMM22 (*16*), PARSE (*17*), and AMBER parm99 (*18*) atomic charge and atomic radius parameters were used for all protein atoms except for the atoms of the metal-coordinated cysteines. The partial charges of +1.28 and −0.82 for the Zn(II) and Cys S^{γ} atoms (PARSE) and +1.28, −0.80, −0.24, and +0.11 for the Zn(II) and Cys S^{γ}, C^{β}, and H^{β} atoms (AMBER), respectively, were adapted from quantum mechanical calculations on the Fe(II)-containing tetramethylthiolate complex (*19, 20*). Partial charges of +1.24, −0.61, −0.38, and +0.09 for the Zn(II) and Cys S^{γ}, C^{β}, and H^{β} atoms, respectively, have been previously optimized for the CHARMM22 parameter set (*21*). The protein termini and the lysine, aspartate, and glutamate residues were set to the charged state. Except as noted, the excess charge of the peptide anions was placed on the nitrogen. A 0.25 Å grid spacing was used with a 40% filling factor. The external dielectric value was set to 78.5, the ionic strength to 0.15 M, the temperature to 25 °C, and the ionic radius to 2.0 Å. For the rotated side chain conformations of Asp 21 and Asp 36, ΔpK calculations were referenced to the peptide anion of Ser 25 for that protein conformation under the assumption that the electrostatic potential at this remote amide will be minimally affected by these side chain rotations.

To examine the structural basis of the differential amide acidities that are predicted using the CHARMM22 parameter set, the charges on specific groups of atoms were set to zero. For the metal binding site, the charges on the Zn and S atoms were set to zero, while the charges on the Cys C^{β} atoms were set to −0.18 to generate a neutral methylene group. Similarly, the charges of the carboxyl carbon and oxygen of the carboxylate groups and the nitrogen and attached hydrogens of the lysine and N-terminal amino groups were set to zero, while the charges on the adjacent carbons were adjusted to generate neutral methylene groups. The backbone can be similarly analyzed taking advantage of the fact that in this parameter set the carbonyl carbon and oxygen have equal and opposite charges, while the N, H^{N}, C^{α}, and H^{α} cluster also has a net neutral charge for the non-proline residues. For proline residues, the charge on C^{δ} is also adjusted to yield the desired net charge.

RESULTS AND DISCUSSION

Hydrogen Exchange of Solvent-Exposed Amides. The experimental data available for the exchange behavior of solvent-exposed protein amides are significantly limited by the fact that the great majority of hydrogen exchange studies have utilized the "exchange-out" technique, in which the protein sample is rapidly transferred to a $^{2}H_2O$-containing buffer, with the disappearance of the amide proton resonances then being monitored by NMR. Under the most common protocols, the amide protons will exchange with deuterium before the first NMR spectrum can be collected unless the exchange rate is at least 1000-fold slower than the reference peptide rate.

Rapid hydrogen exchange can be monitored by magnetization transfer techniques in which the water resonance is selectively excited. The NMR experiment then monitors the transfer of this magnetization to the amide resonances. A particularly robust implementation of magnetization transfer-based hydrogen exchange monitoring is that of CLEANEX-

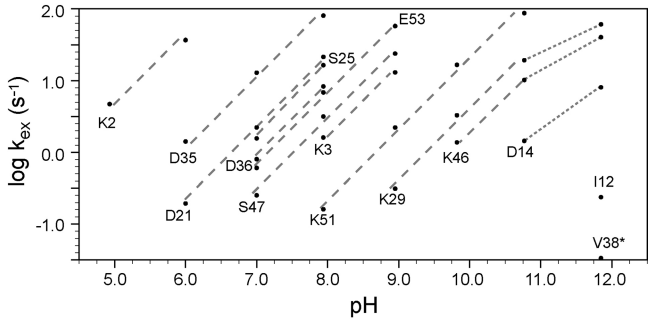

FIGURE 2: Magnetization transfer-based hydrogen exchange rate measurements on the solvent-exposed amides of *Pf* A2K rubredoxin. CLEANEX-PM (*11, 12*) measurements were carried out at 25 °C. Except for the highest-pH interval, dashed lines with a slope of 1.0 were drawn for the pH-dependent data of each solvent-exposed amide, indicating a simple hydroxide ion dependence of the exchange rates over most of the pH range. The exchange rate value for Val 38, marked with an asterisk, is derived by extrapolation from measurements at 52 °C.

PM (*11*) which efficiently suppresses other potential contributions to the observed resonances that are not derived from chemical exchange processes. We have introduced a modification (*12*) to this experiment that compensates for the effects arising from transverse relaxation which limit the accuracy of the deduced exchange rates.

Relaxation-compensated CLEANEX-PM experiments were carried out on a variant of *Pf* rubredoxin with an initial Met-Lys sequence that, unlike the wild-type Met-Ala sequence (*22*), yields homogeneous processing of the N-terminus during expression in *Escherichia coli* (*9*). At each pH, exchange rates can be accurately quantified over the range from 0.2 to 70 s^{-1} (*13*). With the exception of data in the interval of pH 10.77−11.85, the exchange rates of the individual static solvent-accessible amides increase directly with the hydroxide ion concentration (Figure 2). At the highest pH values, the decreased slope for the amides of Lys 29 and Lys 46 presumably reflects the increasingly negative protein charge arising from the neutralization of these amino side chains. Over most of the pH range that was considered, the unit slope found for the correlation between the log exchange rate and the pH indicates that only the dominant charge configuration of *Pf* A2K rubredoxin substantially contributes to the electrostatic environment of the individual amides being monitored.

The data in Figure 2 yield second-order hydroxide-catalyzed rate constants (k_{OH^-}) at 25 °C ranging from $10^{9.68}$ M^{-1} s^{-1} for Lys 2 to $10^{1.55}$ M^{-1} s^{-1} for Ile 12. The exchange of Val 38 at pH 11.85 and 25 °C is too slow to be observed by this method. Taking advantage of the fact that *Pf* rubredoxin is stable up to 94 °C at pH 11.6 (*7*), CLEANEX-PM measurements on the pH 11.85 sample were carried out at modestly elevated temperatures. The exchange rate of 0.37 s^{-1} at 52 °C for Val 38 was extrapolated to 25 °C assuming the same temperature dependence that was observed for Ile 12. The resultant rate constant of $10^{0.67}$ M^{-1} s^{-1} is a billion-fold smaller than that for Lys 2.

Clearly, steric "protection factors" cannot suffice to explain this large range of exchange rates for the solvent-accessible amides. In general terms, the physical basis of this 10^9-fold variation in exchange rate is readily apparent. Although the hydrogen exchange experiment monitors the rate at which a proton is removed from a peptide nitrogen, that rate is directly determined by the thermodynamic acidity of the nitrogen. As observed for O-bound and N-bound hydrogens in general, proton transfer occurs within a hydrogen-bonded collision complex. Furthermore, proton transfer is sufficiently rapid that thermodynamic equilibrium is established before the dissociation of the complex occurs (*23*). More than 35 years ago, Molday and Kallen (*24*) directly demonstrated that peptide ionization behaves like a normal Eigen acid for which the hydroxide-catalyzed exchange rate constant increases with the increasing thermodynamic acidity of the peptide unit, up to the diffusion-limited rate near 2×10^{10} M^{-1} s^{-1} at 25 °C. Altering the electrostatic potential at the amide will (de)stabilize the peptide anion intermediate formed during the exchange reaction and thus shift the thermodynamic acidity of that group. A number of studies (*25–27*) have pointed out the fact that such electrostatic interactions serve to modulate hydrogen exchange rates.

Before turning to the peptide nitrogen acidities on the protein surface, we will consider the smaller-scale variations that occur among simple model peptides that lead to the widely used residue-specific correction factors. These factors vary by up to 8-fold from the reference rates for the alanyl-alanine peptides (*28*). The seemingly most straightforward influence is that of "steric blocking", in which aromatic or branched aliphatic side chains adjacent to the exchanging amide suppress the rate of both hydronium ion- and hydroxide-catalyzed exchange. According to this paradigm (*28*), a bulky side chain physically reduces the rate of access of the catalyst to the amide group. Recently, Avbelj and Baldwin (*29*) offered a more compelling interpretation based on Poisson−Boltzmann continuum electrostatic calculations which indicated that bulky side chains alter the electrostatic solvation free energy of the peptide, thereby thermodynamically suppressing the ionization reactions.

The remainder of the variations observed among the residue-specific correction factors for hydrogen exchange rates have been ascribed to "induction" effects (*28*). McCammon and co-workers (*30*) have applied Poisson−Boltzmann techniques to investigate this phenomenon. Their calculations assumed that the fixed atomic charges of the peptide group were the same for every residue type, and no true chemical induction effects were modeled. These authors found that the residue-specific correction factors arising from the side chain that precedes the exchanging amide could all be predicted within a factor of 2, accounting for the major fraction of the observed variation. Hence, most of the differences in exchange rates among model peptides arise from through-space charge interactions and the resultant solvation effects, rather than from chemical induction effects. These results suggest that the electrostatic properties of all non-proline peptide groups can be considered approximately equivalent, and therefore, their differences in thermodynamic acidity can be predicted from changes in electrostatic potential.

Electrostatic Calculation of Hydrogen Exchange Rates. For pH values of >5, the hydrogen exchange reaction is generally initiated by the removal of an amide hydrogen by an hydroxide ion. Although each amide hydrogen is susceptible to this reaction, the formation of a peptide anion is an exceedingly rare event. With a few significant exceptions (*31*), amide nitrogens are less acidic than the neutral water molecule with its p*K* value of 15.7. As a result, near neutral

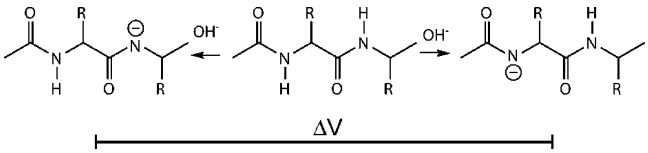

FIGURE 3: Electrostatic solvation free energy of peptide ionization. The reaction of hydroxide ion forms a peptide anion at one site or another along the protein backbone. The differential electrostatic solvation free energy for these two species is given by the product of the charge and the difference in electrostatic potential for the two sites (ΔV) which, in turn, is proportional to the ΔpK for these two amide nitrogens.

pH, the peptide nitrogens are ionized to only roughly ≤ 1 part in 10^{10}. If we compare the two peptide anions illustrated in Figure 3, the difference in free energy between these two states corresponds to the transfer of a proton from one peptide group to the other which is proportional to the ΔpK for those two amide nitrogens. The difference in electrostatic potential between these two sites can be directly estimated by Poisson−Boltzmann continuum electrostatic methods (*32*). This difference in electrostatic potential multiplied by the elementary charge yields the electrostatic solvation free energy. Free energy values are derived from these Poisson−Boltzmann calculations due to the fact that the dielectric constant values assumed for the bulk solvent and protein interior represent an averaging of the dynamic response of the protein and the solvent molecules to the electrostatic charge environment.

The use of hydrogen exchange to determine peptide nitrogen p*K* values offers a number of practical advantages as a means of assessing the performance of electrostatic modeling calculations. Given the high p*K* values for the peptide group, the extremely small fraction of ionization of the monitored amide does not discernibly influence the ionization equilibria of the protein side chains or that of other amides near neutral pH. As a result, in contrast to the more familiar electrostatic calculation of side chain titration behavior, the side chain ionizations are effectively decoupled from the ionization of the amide so that there is no need to iteratively calculate the free energy effect of ionizing the target amide on the charge distribution of the rest of the protein. Conversely, the electrostatic free energies of the neutral and anionic amide species are both dependent on the same equilibrium side chain charge distribution. An additional practical benefit results from focusing on differential p*K* effects in this analysis. Since the two protein structures modeled differ only by the placement of a single proton on one peptide group or the other, the technical complications that arise from the grid self-energy contribution to the total calculated energy cancel out. Furthermore, the overall charge state of the system remains the same in each such calculation so that various numerical uncertainties are minimized.

Successful Poisson−Boltzmann prediction of hydrogen exchange rates for the solvent-exposed amides of *Pf* A2K rubredoxin requires that the exchange occur from the conformation assumed in the calculation. The X-ray structure indicates that the amide proton corresponding to Lys 2 is hydrogen bonded to a carboxylate oxygen of the Glu 15 side chain, yet the hydroxide-catalyzed exchange rate constant (k_{OH^-}) for this amide is only ~4-fold lower than the diffusion-limited value, indicating that the p*K* value for this amide has nearly reached that for the ionization of water. The exchange rate of Lys 2 agrees with the corresponding model

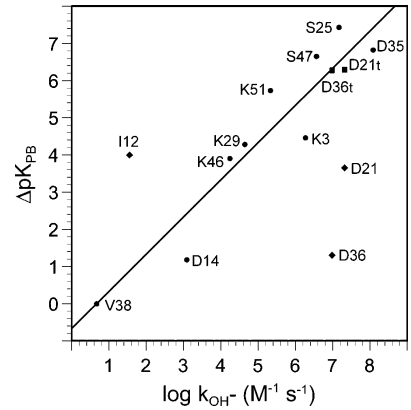

FIGURE 4: Correlation of *Pf* A2K rubredoxin hydrogen exchange rate constants with Poisson−Boltzmann-derived ΔpK values (electrostatic solvation free energy in units of kT/ln[10]) using CHARMM22 electrostatic parameters with an internal dielectric constant of 3 at 25 °C. ΔpK values for the Asp 21 and Asp 36 amides were predicted for the X-ray-determined conformation (◆) and with these side chains (■) reoriented trans to the backbone amide (χ_1 of 180°). The seemingly anomalous Ile 12 amide (◆) lies closest to the tetrathiolate-coordinated metal site. Among the solvent-exposed amides, Ile 12 is the most sensitive to the charge state of that metal. The root-mean-square deviation (rmsd) for the unit slope correlation between the predicted ΔpK values and the hydrogen exchange data for the other 11 solvent-accessible amides is 0.78 pH unit.

peptide value, which reflects the accelerating effect of the adjacent positively charged N-terminus. The rapid exchange rate of Lys 2 suggests fraying at the N-terminus of *Pf* A2K rubredoxin, as previously noted in the solution structural analysis (*33*). Variants of *Pf* rubredoxin that retain the N-terminal methionine are less stable than the wild-type protein by 1.5 kcal/mol (*6, 34, 35*). A similar dynamical fraying also appears to occur for Glu 53 at the C-terminus. In the X-ray structure, both Asp 21 and Asp 36 have one of their carboxylate oxygens within 3 Å of their own amide proton. This proximity will strongly destabilize the peptide anion exchange intermediate. Since rotation of the χ_1 side chain dihedral angle appears to be unimpeded for both residues, we also performed calculations with the carboxylates being oriented trans to the amide nitrogen (i.e., χ_1 of 180°).

DelPhi (*15*) was used to estimate the electrostatic potential at each of the 12 solvent-exposed amides that are not hydrogen bonded to a main chain carbonyl oxygen in the analogous rubredoxin X-ray structure (PDB entry 1BQ8) (*4*). After setting all the side chain and C-terminal carboxyls as well as the side chain and N-terminal amines to the ionized form, we removed the amide proton for each of these 12 residues one at a time and calculated the electrostatic solvation free energy for each species.

When the atomic charge and atomic radius values of the CHARMM22 parameter set (*16*) and an internal dielectric constant value of 3 were applied to the 12 peptide anion species of the solvent-exposed amides, the majority of the calculated ΔpK values fall near a unit slope correlation with the second-order exchange rate constants that were obtained from the data of Figure 2, indicating the changes in peptide nitrogen acidity inferred from the experimental hydrogen exchange are reasonably well predicted from the Poisson−Boltzmann calculations of thermodynamic acidity (Figure 4).

In Figure 4, it can be seen that the estimated Δp*K* values for the amides of Asp 21 and Asp 36 with their side chains positioned as in the X-ray structure lie substantially below the correlation with hydrogen exchange rates observed for the other solvent-exposed amides. For these two residues, the predicted weak amide acidity arises from the placement of the intraresidue carboxylate near the amide hydrogen, as noted above. As the trans rotamers of these side chains appear to be energetically readily accessible, the population in this side chain conformation will contribute to a much more favorable predicted electrostatic solvation free energy.

The correlation between the hydrogen exchange rate constant and the predicted electrostatic potential for Ile 12 also deviates markedly from the correlation observed for the other solvent-exposed amides. A plausible explanation for the anomalous behavior of this residue may arise from the fact that the amide of Ile 12 is 7.3 Å from the center of the tetrathiolate metal site, significantly closer to that site than are any of the other amides illustrated in Figure 4. Substitution of Ga(III) or Ge(IV) for diamagnetic Zn(II) in the *Pf* A2K rubredoxin metal site yields an up to 1 million-fold acceleration in the exchange of nearby amides (*36*). The distance dependence of these metal charge-dependent effects closely correlates with the predicted differential electrostatic potentials at the amide nitrogen sites (*37, 38*). Substitution of Ge(IV) yields a tetrathiolate metal binding site with a net charge of zero (*39*) which increases the rate of Ile 12 exchange by 800-fold, an increase substantially greater than that for any of the other solvent-exposed amides (*36*). The anomalous behavior of Ile 12 exchange in Figure 4 may indicate that these electrostatic calculations do not adequately represent the dielectric shielding of the metal site charge.

Including the Asp 21 and Asp 36 side chains in their trans rotamer conformations, these electrostatic potential calculations predict the variations in hydrogen exchange rate constants for 11 solvent-exposed amides that vary over a range of more than 10^7, with a rmsd of 0.78 pH unit (Figure 4). These p*K* estimations were derived from the nonlinear Poisson−Boltzmann equation. However, the simpler linear equation yielded a maximal change for the individual Δp*K* values of only 0.2 unit. In terms of accuracy, these predictions of hydrogen exchange rate constants compare quite favorably with analogous predictions of p*K* values for protein side chains (*40–42*), while the range of differential p*K* values monitored by hydrogen exchange is substantially broader.

Dependence on the Effective Dielectric of the Protein Interior. The sensitivity of the predicted *Pf* A2K rubredoxin exchange rates to the effective dielectric of the protein interior was examined by carrying out electrostatic calculations for a range of internal dielectric values. With a dielectric constant of 2, the correlation between the exchange rate constants and the calculated p*K* values for the 11 solvent-exposed amides yielded a rmsd value from the unit slope correlation that was twice as large as that for an internal dielectric constant of 3 (Figure 5A). The Poisson−Boltzmann calculations predict a markedly stronger variation in the amide nitrogen p*K* values than is inferred from the hydrogen exchange data. The slope of the best fit line in this log−log plot is 1.49, implying that the differences in thermodynamic acidity are predicted to be substantially larger than the corresponding experimental differences in kinetic acidity.

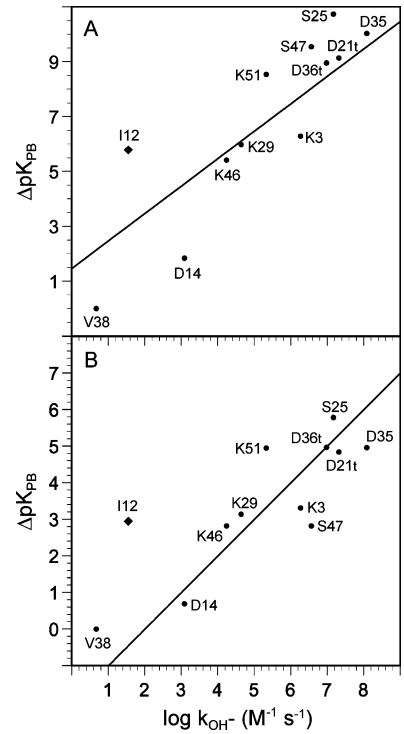

FIGURE 5: Internal dielectric constant dependence for the correlation of hydrogen exchange rate constants with predicted Δp*K* values for *Pf* A2K rubredoxin. Calculations were carried out using CHARMM22 atomic charge and atomic radius parameters. (A) Correlation with an internal dielectric value of 2. The systematic deviations from the line of slope of 1.0 indicate that the variation in the predicted Δp*K* values spans a wider range than the Δp*K* values inferred from the hydrogen exchange data, suggesting that the differential electrostatic potentials are overestimated. (B) Correlation with an internal dielectric value of 4. The variations in the electrostatic potential appear to be underestimated, relative to the hydrogen exchange data, as indicated by the slope of the best fit line being 0.77 rather than the unit slope correlation line given in the figure.

These exaggerated differences in the predicted electrostatic potential are consistent with an underestimation of the dielectric shielding within the protein interior. Use of an internal dielectric constant of 4 also resulted in an increased scatter from the unit slope correlation line (Figure 5B) and yielded a reduced variation in the electrostatic potential at the amide nitrogens. In this case, the slope of the best fit line is 0.77, consistent with an overestimation of the dielectric shielding effect of the protein.

Analyses of side chain p*K* values have yielded a wide range of estimates for the effective dielectric constant of the protein interior (*40, 42, 43*). In part, this variability arises from a limited experimental sensitivity to the dielectric shielding effect of the protein, reflecting the fact that these ionizable groups are most often highly solvated and physically removed from the protein interior. In addition, the conformations of most ionizable side chains are often less well defined than the backbone conformation in X-ray structures. Furthermore, structures are usually available for only one of the charge states of a given side chain, and most electrostatic calculations assume equivalent structures for both charge states. Multiconformation continuum electrostatic (MCCE) calculations (*44*) may help address the latter limitation. However, particularly for buried ionizable side chains, adequate structural representation of the charged state of the side chain remains a substantial problem.

As a result of the diffusion-limited rate at which H^+ and OH^- react with the neutral forms of the ionizable side chains, both the neutral and charged states for these side chains have lifetimes in the range of microseconds to milliseconds near pH 7. This lengthy time period allows for extensive structural dielectric relaxation by the protein in the charged state that is particularly relevant for the ionization of buried side chains. Questions regarding penetration of solvating water molecules (*45*) or transient partial unfolding (*46*) for such a charged side chain state are difficult to resolve, yet these structural alterations must be characterized to accurately model the electrostatic interactions.

In the overwhelming majority of cases, protein amide nitrogens are less acidic than water. Therefore, in marked contrast to the situation for ionizable side chains, it is the reverse reaction in which a neutral water molecule donates a proton to the peptide anion that occurs at a diffusion-limited rate. The lifetime of the peptide anion intermediate is comparable to the dominant Debye relaxation time for water (8 ps) (*47*). The highly transient nature of the peptide anion strongly limits the time frame for the dielectric response of the protein to this ionization (*38*). Changes in the charge state of the protein side chains occur far too slowly to yield a dielectric response to peptide ionization. This is the kinetic correlate of the thermodynamic decoupling of the amide and side chain ionizations that was discussed above. In addition, protein conformational transitions that occur more slowly than the lifetime of the peptide anion cannot significantly contribute to the dielectric environment sensed by that anion. Even the comparatively unrestricted transitions between side chain rotamers for surface residues (*48, 49*) occur at rates that are 10^1-10^2-fold slower than would appear to be required for making a significant contribution to the dielectric relaxation that occurs in response to peptide anion formation. The restricted mobility of the backbone, in combination with the brief time window for the dielectric response to the ionization of the peptide nitrogen, implies that the structure surrounding the peptide anion should often be represented well by that of the un-ionized state.

Dependence on Atomic Charge Parameterization. To test the sensitivity of these electrostatic calculations to the assumed atomic charge and atomic radii, the parameter sets from the PARSE and AMBER force fields were applied with an internal dielectric value of 3. The correlation for the PARSE parameters between the predicted ΔpK values and the experimental hydrogen exchange rates was qualitively similar to the correlation that was obtained for the CHARMM22 parameters, indicating a similar effective internal dielectric (Figure 6A). However, the quality of the correlation is appreciably reduced, with the PARSE parameters yielding a rmsd value of 1.28 pH units. The AMBER parm99 atomic charge and radius parameters yielded a decidedly weaker correlation than either of the other two parameter sets (Figure 6B).

The utility of hydrogen exchange data for distinguishing among electrostatic models need not be limited to those currently incorporated into the familiar nonpolarizable force fields. Experimental data on electrostatic potentials along the protein−solvent interface should prove to be valuable in optimization of more physically realistic polarizable electrostatic force fields that are currently under development (*50, 51*).

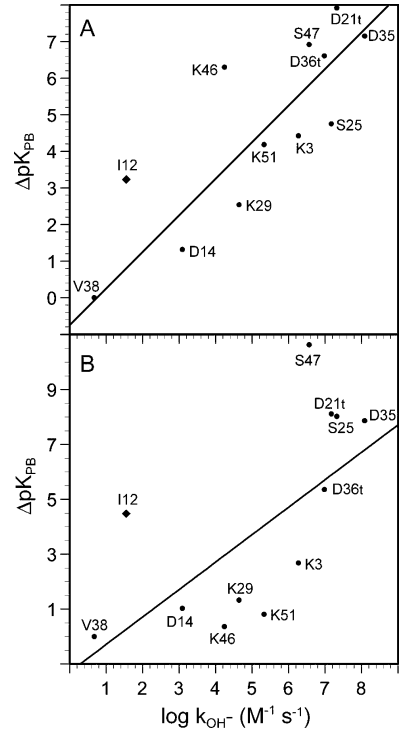

FIGURE 6: Correlation of *Pf* A2K rubredoxin hydrogen exchange rate constants with ΔpK values derived using PARSE and AMBER parm99 electrostatic parameters. Calculations were carried out as described in the legend of Figure 4. (A) The PARSE atomic charge and atomic radius parameters yielded a rmsd of 1.28 pH units from the unit slope correlation. (B) A weak correlation between the hydrogen exchange rate constants and Poisson−Boltzmann-derived ΔpK values was obtained with the parm99 electrostatic parameter set with a rmsd of 2.46 pH units from the unit slope correlation.

All of the Poisson−Boltzmann calculations summarized in Figures 4–6 assume that the excess negative charge of the peptide anion is placed on the amide nitrogen. The electrostatic modeling of hydrogen exchange in simple peptides by McCammon and co-workers (*30*) compared calculations in which the excess charge was placed either exclusively on the amide nitrogen, exclusively on the carbonyl oxygen, or equally shared between these two atoms. These authors concluded that placing the excess charge on the amide nitrogen yielded the best fit to the experimental data. We carried out electrostatic calculations on *Pf* A2K rubredoxin with the excess charge equally shared between the amide nitrogen and oxygen (Figure 7). Although the overall correlation between the predicted differential electrostatic free energies and the hydrogen exchange data was preserved, the spread from the unit slope correlation was nearly 2-fold larger than that obtained when the excess negative charge is confined to the amide nitrogen (Figure 4).

For these calculations on *Pf* rubredoxin, the apparent localization of the excess charge on the amide nitrogen may be justified, in part, by consideration of solvent exposure. For the 12 solvent-exposed amides considered in Figures 4–7, the carbonyl oxygens of those peptide linkages are substantially exposed to solvent (>2 Å^2) only for residues Pro 20 and Asp 35. As indicated in Figure 8, for the ionization of the corresponding amides, Asp 21 and Asp 36, there is only a small energy difference between localization of the excess charge on the amide nitrogen and equal sharing with the carbonyl oxygen. In contrast, placement of the excess charge on the nitrogen is between 5 and 10 kT (~3−6 kcal/mol) more favorable for nearly all of the other solvent-exposed

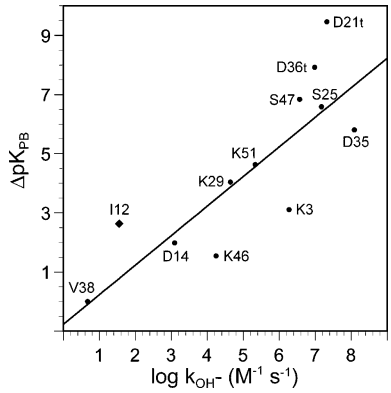

FIGURE 7: Correlation of *Pf* A2K rubredoxin hydrogen exchange rate constants with Poisson−Boltzmann-derived Δp*K* values with the excess charge of the peptide anion shared equally between the nitrogen and the carbonyl oxygen. Other parameters were applied as described in the legend of Figure 4. The electrostatic calculations assuming equal sharing of the excess charge between the nitrogen and carbonyl oxygen predict the experimental kinetic acidities with a rmsd of 1.49 pH units.

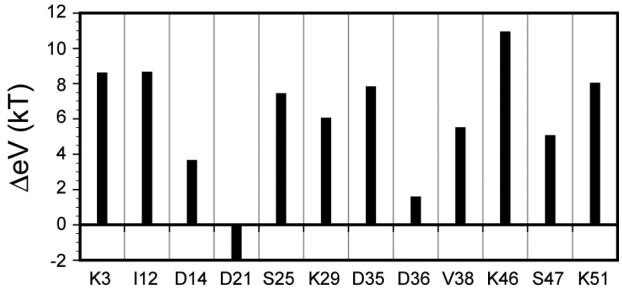

FIGURE 8: Energy difference for placement of the peptide anion excess charge on the amide nitrogen vs equal sharing with the carbonyl oxygen. Poisson−Boltzmann continuum electrostatic calculations were carried out for each solvent-exposed amide position in *Pf* rubredoxin using the CHARMM22 electrostatic parameters with an internal dielectric constant of 3. The trans χ_1 rotamer side chain conformation was utilized for the Asp 21 and Asp 36 rotamers. With the exception of Asp 21, equal sharing of the excess charge between the amide nitrogen and the carbonyl oxygen yields a less favorable electrostatic free energy for each residue.

amides. In these cases, the carbonyl oxygen is in a substantially lower dielectric environment so that displacement of the excess negative charge toward the solvent interface is strongly favored.

Structural Basis of the Differences in Amide Nitrogen Acidity for Pf Rubredoxin. Given the robust prediction of the *Pf* rubredoxin hydrogen exchange rates provided by Poisson−Boltzmann calculations utilizing the CHARMM22 electrostatic parameter set with an internal dielectric constant of 3, this modeling was used to further examine how specific structural elements contribute to the observed range of amide acidities. By setting all of the atomic charges to zero while retaining the atom sizes that define the molecular volume, one can estimate the contribution to differential amide acidity arising from the protein dielectric shielding for a negative charge placed at each amide nitrogen. It should be noted that such a calculation provides the reference state for deriving the generalized Born radii which are widely used to approximate the effective structural burial of each protein atom in rapid calculations of electrostatic interactions for which the comparatively slow Poisson−Boltzmann techniques are too cumbersome (*52*). In Figure 9, the differential

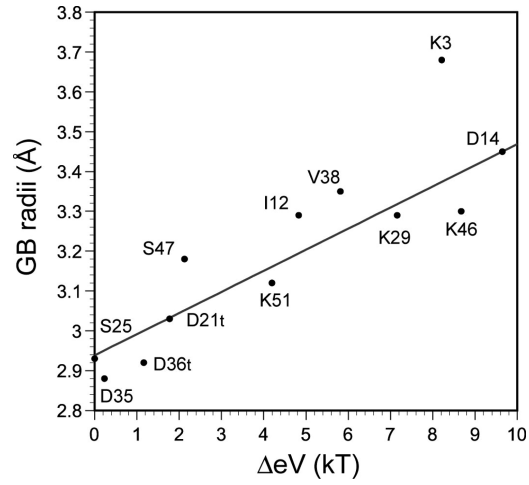

FIGURE 9: Contribution of the internal dielectric to the differential acidities of the solvent-exposed amides of *Pf* rubredoxin. With all protein atomic charges set to zero, an internal dielectric constant value of 3 gives rise to a 10 kT (∼6 kcal/mol) range of electrostatic solvation free energies for the solvent-exposed peptide anions. The generalized Born radius provides an alternate characterization of the effective degree of structural burial. With the exception of Lys 3, the Model I algorithm (*53*) for estimating generalized Born radii correlates fairly closely with the internal dielectric contribution to the differential acidities. The Model II algorithm proposed in that study yielded an equivalent quality of fit.

solvation free energies of the peptide anions for the solvent-exposed amides are compared to the corresponding generalized Born radii estimated via a current protocol (*53*).

As is apparent in Figure 1, the amide of Val 38 lies on a locally concave section of the protein surface so that a relatively large proportion of the surrounding volume is occupied by protein atoms. In contrast, the amide of Ser 25 is more extensively surrounded by the aqueous phase. As a result, the internal protein dielectric (ϵ) of 3 gives rise to a differential electrostatic solvation free energy of 6 kT for the Val 38 peptide anion, which corresponds to $^1/_3$ of the overall difference in predicted acidity with respect to the Ser 25 amide. On the other hand, analogous calculations (Figure 9) for the amides of Lys 3, Asp 14, Lys 29, and Lys 46 all predict a significantly larger differential electrostatic solvation free energy arising from the internal protein dielectric which constitutes a much larger fraction of the overall predicted difference in acidities for these residues.

The differential electrostatic solvation free energy contributions arising from the protein atomic charges can be analyzed by systematically adding these interactions. In Figure 10 are summarized the differential electrostatic solvation free energies, relative to the Ser 25 amide, that result from the bulk protein dielectric of 3 (blue), from the neutral backbone partial charges (orange), from the neutral side chain partial charges (green), from all formal charges (red), and finally from the overall differential electrostatic solvation free energy (black) for each solvent-exposed amide. It is immediately apparent that the relative contributions to the overall differential amide acidities vary dramatically among the individual residues. In comparison to the Ser 25 reference, the decrease in amide acidity that arises from the internal dielectric of 3 is largely offset by favorable interactions between the peptide anion and the partial charges of the backbone for residues Ile 12, Asp 21, Ser 47, and Lys 51. In the case of Ile 12, interactions between the peptide

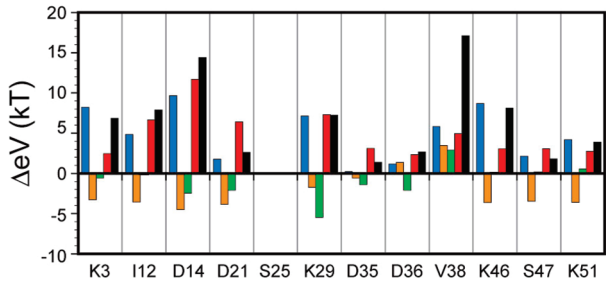

FIGURE 10: Differential electrostatic solvation free energy contributions arising from the protein atomic charges. For each residue, the change in amide acidity, relative to Ser 25, that arises solely from an internal dielectric constant value of 3 is indicated in blue. In orange is indicated the increment in differential electrostatic solvation energy due to the peptide backbone atomic charges. The increment arising from the side chain atomic charges, not including formal charges, is indicated in green. In red is given the increment due solely to formal charges, while in black is indicated the total electrostatic solvation free energy difference with respect to Ser 25.

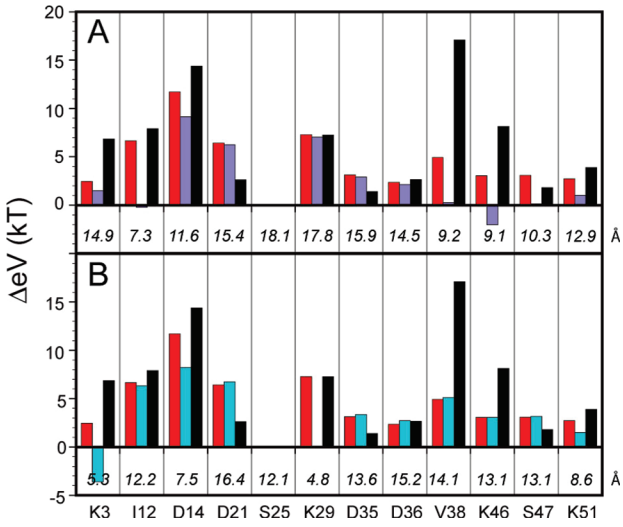

FIGURE 11: Differential electrostatic solvation free energy arising from the buried formal charges of *Pf* rubredoxin. The increments due to all formal charges and to the total electrostatic solvation free energy, relative to the Ser 25 amide, are indicated in red and black as in Figure 10. Indicated with purple in panel A is the formal charge contribution to the electrostatic solvation free energy in which the charge on the Zn(II)-tetrathiolate binding site is set to zero. Similarly, in panel B the changes in the amide acidities that arise from all formal charges, except that for the Glu 15 side chain, are given in cyan. The distances from each amide nitrogen to the metal and to the nearest carboxylate oxygen of Glu 15 are given in angstroms.

anion and the formal charges of the protein dominate the overall differential amide acidity as the electrostatic interactions with the other side chain partial charges appear to make a negligible contribution. In marked contrast, such side chain partial charge interactions enhance the relative acidity of the Lys 29 amide by 5.5 kT (2.4 pH units).

More detailed interpretations can be provided by modulating individual interactions in the Poisson−Boltzmann calculations. A large increase in acidity is predicted for the amides of Ile 12, Val 38, and Lys 46 when the −2e charge at the Zn(II)-tetrathiolate binding site is neutralized (Figure 11A). Of the five solvent-exposed amides of *Pf* rubredoxin for which exchange rates were observed as a function of Zn(II), Ga(III), and Ge(IV) substitution in conventional isotope exchange-out experiments (*36*), only these three residues exhibited significantly accelerated exchange rates as the charge on the metal binding site was decreased. As might be expected, the solvent-exposed amides that lie along the surface of the protein opposite to that of the metal binding site (i.e., Asp 21, Lys 29, Asp 35, and Asp 36, and the Ser 25 reference amide) predict a negligible effect of neutralizing the metal site, which was observed for Lys 29 in the metal substitution study (*36*). Overall, potentially discernible effects of the charge on the metal binding site are predicted to extend out approximately 14 Å from the Zn(II) center.

The hyperthermophilic rubredoxin contains a structurally buried Glu 15 side chain which is not observed among the homologous mesophilic rubredoxins. The interactions of this side chain have been proposed to play a significant role in the striking thermostability of this protein (*54*). Setting the formal charge of this side chain to zero yields variations in the predicted acidity of the solvent-exposed amides (Figure 11B) that are more spatially limited than those observed for the metal binding site. The amide acidities of Lys 3 and Lys 29 increase dramatically upon neutralization of the Glu 15 carboxylate, along with a smaller increase predicted for Asp 14. Each of these three amide nitrogens is within 7.5 Å of this buried carboxylate. In contrast, the acidities for the remainder of the solvent-exposed amides are predicted to have little dependence on the Glu 15 carboxylate charge. The more limited spatial extent of the electrostatic effects arising from the Glu 15 side chain, as compared to those of the metal site, reflects both the 2-fold smaller net charge and the less buried position of this carboxylate.

Neutralization of the charge at the metal site causes the predicted acidity of Lys 46 to increase above that predicted when all the formal charges of the protein are neutralized (Figure 11A). Hence, there must be an additional charge interaction that serves to stabilize the peptide anion of this residue. Indeed, neutralizing the ϵ-amino group of its own side chain predicts a 3 kT stabilization. Similarly, neutralization of the Glu 15 side chain indicates the presence of additional formal charge interactions that stabilize the peptide anion of Lys 3 (Figure 11B). Once again, neutralizing the ϵ-amino group of its own side chain is predicted to significantly reduce the acidity of the Lys 3 amide.

Only four other solvent-exposed amides predict appreciable formal charge-dependent changes in acidity that are not due to either the metal site or the Glu 15 side chain. The amides of Asp 21, Asp 35, and Asp 36 are all virtually unaffected by the charge state of either the metal site or Glu 15. The 6.4 kT increase in electrostatic solvation free energy predicted for the peptide anion of Asp 21 can be largely ascribed to neutralization of its own side chain (3.4 kT) and to neutralization of the nearby Asp 19 side chain (4.0 kT). Similarly, neutralization of their own side chain carboxylates predicts increases in acidity corresponding to 3.5 and 3.8 kT for Asp 35 and Asp 36, respectively. Although the amide acidity of Asp 14 is sensitive to the charge state of both the metal binding site and the Glu 15 side chain, its greatest sensitivity to the formal charges arises from its own side chain (8.4 kT).

For the majority of the solvent-exposed amides of *Pf* rubredoxin, the peptide acidity shows little sensitivity to the electrostatic effects of the side chain atoms which do not bear a formal charge. The most noteworthy exception is the amide of Lys 29 for which such interactions substantially

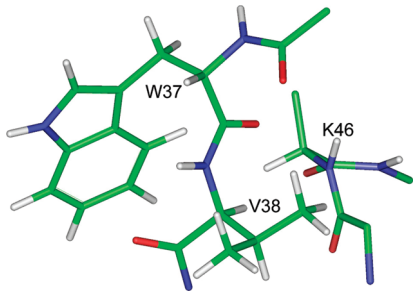

FIGURE 12: Electrostatic environment of the Val 38 peptide group. The negative end of the Trp 37 indole N−H dipole is oriented toward the Val 38 amide nitrogen. The carbonyl oxygen of Trp 37 is nearly solvent inaccessible (0.3 Å^2), yet it forms no intramolecular hydrogen bond.

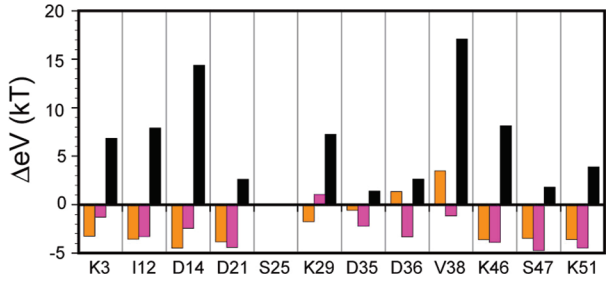

FIGURE 13: Amide acidity contributions arising from the adjacent backbone peptide units. The increments in differential electrostatic solvation free energy arising from all backbone partial charges and the total electrostatic solvation free energy, relative to the Ser 25 amide, are indicated in orange and black, respectively, as in Figure 10. In magenta are illustrated the increments in differential electrostatic solvation free energy that are due to the tripeptide of the backbone that is centered on the ionizing amide.

stabilize the peptide anion (Figure 10). The carbonyl oxygen of Thr 28 from that same peptide group is hydrogen bonded to the phenolic hydroxyl of Tyr 13 which accounts for 2.2 kT of this stabilization.

Val 38 is the only residue for which the side chain atoms that lack a formal charge give rise to a significant destabilization of the peptide anion (Figure 10). Approximately two-thirds of this effect arises from the charge distribution in the pyrrole ring component of the Trp 37 side chain for which the negative end of the indole N−H dipole is oriented toward the Val 38 amide nitrogen (Figure 12).

The dependence of the amide acidities on the partial charges of the protein backbone can be further dissected by analyzing the contribution that arises from the local segment extending to the next peptide unit on either side of the ionizing peptide group. To carry out the differential Poisson−Boltzmann calculations in a manner similar to the manner of those described above, for each amide ionization studied, the partial charges of the analogous segment surrounding the Ser 25 amide are also included, and the electrostatic solvation free energy for ionization of the Ser 25 amide is also calculated. As seen from the data depicted in Figure 13, for the majority of solvent-exposed amides the immediately neighboring peptide groups largely account for the overall variation in amide acidity arising from the partial charges of the protein backbone. In contrast, relative to the Ser 25 amide reference, the full backbone partial charge set predicts a nearly 5 kT (~3 pH unit) suppression of the amide acidities for Asp 36 and Val 38 that is in excess of the contribution arising from the neighboring peptide groups. With the exception of these two residues, the carbonyl oxygen in every peptide linkage of the solvent-exposed amides forms an intramolecular hydrogen bond. The carbonyl oxygen of Asp 35 is fully exposed to the solvent phase, while as indicated in Figure 12, the carbonyl oxygen of Trp 37 is almost completely buried but lacks any hydrogen bond donor. As noted above, the carbonyl oxygen of Thr 28 forms a hydrogen bond to the phenolic hydroxyl of Tyr 13, while all other solvent-exposed amides of *Pf* rubredoxin form hydrogen bonds between their carbonyl oxygens and other backbone amides of the protein.

Despite the strikingly slow exchange rate exhibited by Val 38, the only relatively exceptional structural characteristic of this residue is that the carbonyl oxygen of that peptide group is nearly solvent inaccessible but not hydrogen bonded. In marked contrast to the other solvent-exposed amides of *Pf* rubredoxin, each of the major classes of electrostatic interactions contributes to the differential solvation free energy of the Val 38 amide in the direction of reduced peptide acidity (Figure 10).

Pf A2K rubredoxin has solvent-exposed amides that exchange more slowly than even the most strongly protected amides in many of the proteins that have been reported to date. If such a protein were to exhibit a local electrostatic environment around one of its exposed amides such that electrostatic calculations predict a p*K* value similar to that of *Pf* A2K rubredoxin Val 38, the observed hydrogen exchange rate could not match that prediction, since global unfolding would provide a more efficient path for exchange. For the hydrogen exchange rate of a solvent-exposed amide to match the electrostatic prediction of acidity, at minimum it should be expected that either one or both of the adjacent amides will have hydrogen exchange rates that are equal to or slower than the rate for the amide of interest. The fact that this condition is met for each of the slowly exchanging solvent-exposed amides of *Pf* A2K rubredoxin is consistent with a preservation of the nativelike topology in the neighborhood of that site for a sufficient fraction of the time, so exchange from this conformation dominates the observed kinetics.

The demonstration that continuum dielectric calculations can usefully predict hydrogen exchange rates for solvent-exposed amides enhances the ability to interpret the electrostatic potential-dependent modulation of the hydrogen exchange behavior of structurally buried amides as well. As noted above, substituting Ga(III) or Ge(IV) for Zn(II) in the active site of *Pf* rubredoxin yields increases in the exchange rates for nearby amide hydrogens of up to a million-fold (*36*). The metal charge-dependent differences in the apparent peptide acidities of the buried amides were found to vary inversely with the distance between the metal and the amide nitrogen positions in the X-ray structure. Although this simple isotropic Coulomb's law dependence ignores the difference between the dielectric shielding properties of the protein and the bulk solvent phase, it clearly illustrates the direct electrostatic basis of the metal charge-dependent differential hydrogen exchange rates. Our (*37, 38*) subsequent Poisson−Boltzmann analyses of these hydrogen exchange data indicated an effective protein internal dielectric constant value of 6. On one hand, the ability to use the high-resolution X-ray structure of *Pf* rubredoxin to faithfully predict the

metal charge-dependent differences in the hydrogen exchange of the buried amides demonstrates that these exchange reactions must occur from conformations that closely resemble the native structure. On the other hand, since the solvent must access these buried amides to carry out the exchange reaction, the resultant conformational transitions and local hydration can be expected to give rise to an effective dielectric shielding greater than what might be expected for a comparatively rigid surface-exposed amide in the native conformation (*36, 38*). Our observation, presented here, of an effective internal dielectric constant value of 3 for the solvent-exposed sites that require no conformational transition for exchange supports our earlier interpretation of the metal charge-dependent effects on hydrogen exchange in this protein.

CONCLUSION

Recognition of the fact that the peptide nitrogens along the protein backbone act as normal Eigen acids enables the use of kinetic measurements of hydrogen exchange in monitoring the thermodynamic acidities of these sites and, in turn, in characterizing the electrostatic properties along the protein−solvent interface. Modulation of the local electrostatic potential across the surface of *Pf* A2K rubredoxin alters the ionization reaction of the solvent-exposed amides by a factor of 10^9. Within the limits of the assumptions of the nonpolarizable atomic charge CHARMM22 parameter set and uniform dielectric constants for both protein and solvent, the variations in the hydrogen exchange rates of these solvent-exposed amides can be interpreted on a detailed structural basis. The striking heterogeneity in the electrostatic properties that is observed along the protein−solvent interface should prove fruitful in efforts to understand the magnitude of catalytic acceleration which remains a major challenge in the field of chemical enzymology (*55*).

ACKNOWLEDGMENT

We acknowledge the use of the Wadsworth Center NMR facility and the technical assistance of Lynn McNaughton.

SUPPORTING INFORMATION AVAILABLE

A table showing the hydrogen exchange rates of the solvent-exposed amides of *Pf* A2K rubredoxin as a function of pH (Table S1). This material is available free of charge via the Internet at http://pubs.acs.org.

REFERENCES

1. Huyghues-Despointes, B. M. P., Pace, C. N., Englander, S. W., and Scholtz, J. M. (2001) Measuring the Conformational Stability of a Protein by Hydrogen Exchange. In *Protein Structure, Stability and Folding* (Murphy, K. P., Ed.) Vol. 168, pp 69−92, Humana Press, Totowa, NJ.
2. Li, R., and Woodward, C. (1999) The hydrogen exchange core and protein folding. *Protein Sci. 8*, 1571–1591.
3. Bai, Y. W., Milne, J. S., Mayne, L., and Englander, S. W. (1994) Protein Stability Parameters Measured by Hydrogen Exchange. *Proteins: Struct., Funct., Genet. 20*, 4–14.
4. Bau, R., Rees, D. C., Kurtz, D. M., Scott, R. A., Huang, H. S., Adams, M. W. W., and Eidsness, M. K. (1998) Crystal-structure of rubredoxin from *Pyrococcus furiosus* at 0.95 Å resolution, and the structures of N-terminal methionine and formylmethionine variants of *Pf* Rd. Contributions of N-terminal interactions to thermostability. *J. Biol. Inorg. Chem. 3*, 484–493.
5. Lee, B., and Richards, F. M. (1971) The Interpretation of Protein Structures: Estimation of Static Accessibility. *J. Mol. Biol. 55*, 379–400.
6. LeMaster, D. M., Tang, J., and Hernández, G. (2004) Absence of Kinetic Thermal Stabilization in a Hyperthermophile Rubredoxin Indicated by 40 Microsecond Folding in the Presence of Irreversible Denaturation. *Proteins 57*, 118–127.
7. Hiller, R., Zhou, Z. H., Adams, M. W. W., and Englander, S. W. (1997) Stability and dynamics in a hyperthermophilic protein with melting temperature close to 200 °C. *Proc. Natl. Acad. Sci. U.S.A. 94*, 11329–11332.
8. Anderson, D. E., Lu, J., McIntosh, L., and Dahlquist, F. W. (1993) T4 Lysozyme. In *NMR of Proteins* (Clore, G. M., and Gronenborn, A. M., Eds.) pp 258−304, CRC Press, Boca Raton, FL.
9. Tang, J., Hernández, G., and LeMaster, D. M. (2004) Increased peptide deformylase activity for the N-formylmethionine processing of proteins overexpressed in *Escherichia coli*: Application to homogeneous rubredoxin production. *Protein Expression Purif. 36*, 100–105.
10. Hernández, G., and LeMaster, D. M. (2001) Reduced temperature dependence of collective conformational opening in a hyperthermophile rubredoxin. *Biochemistry 40*, 14384–14391.
11. Hwang, T. L., van Zijl, P. C. M., and Mori, S. (1998) Accurate Quantitation of Water-Amide Proton Exchange Rates using the Phase-Modulated CLEAN chemical EXchange (CLEANEX-PM) Approach with a Fast-HSQC (FHSQC) Detection Scheme. *J. Biomol. NMR 11*, 221–226.
12. Hernández, G., and LeMaster, D. M. (2003) Relaxation compensation in chemical exchange measurements for the quantitation of amide hydrogen exchange in larger proteins. *Magn. Reson. Chem. 41*, 699–702.
13. LeMaster, D. M., Tang, J., Paredes, D. I., and Hernandez, G. (2005) Enhanced thermal stability achieved without increased conformational rigidity at physiological temperatures: Spatial propagation of differential flexibility in rubredoxin hybrids. *Proteins 61*, 608–616.
14. Word, J. M., Lovell, S. C., Richardson, J. S., and Richardson, D. C. (1999) Asparagine and Glutamine: Using Hydrogen Atom Contacts in the Choice of Side-chain Amide Orientation. *J. Mol. Biol. 285*, 1733–1747.
15. Rocchia, W., Sridharan, S., Nicholls, A., Alexov, E., Chiabrera, A., and Honig, B. (2002) Rapid Grid-based Construction of the Molecular Surface and the Use of Induced Surface Charge to Calculate Reaction Field Energies: Applications to the Molecular Systems and Geometric Objects. *J. Comput. Chem. 23*, 128–137.
16. MacKerell, A. D., Jr., Bashford, D., Bellott, M., Dunbrack, R. L., Jr., Evanseck, J. D., Field, M. J., Fischer, S., Gao, J., Guo, H., Ha, S., Joseph-McCarthy, D., Kuchnir, L., Kuczera, K., Lau, F. T. K., Mattos, C., Michnick, S., Ngo, T., Nguyen, D. T., Prodhom, B., Reiher, W. E., Roux, B., Schlenkrich, M., Smith, J. C., Stote, R., Straub, J., Watanabe, M., Wiorkiewicz-Kuczera, J., Yin, D., and Karplus, M. (1998) All-Atom Empirical Potential for Molecular Modeling and Dynamics Studies of Proteins. *J. Phys. Chem. B 102*, 3586–3616.
17. Sitkoff, D., Sharp, K. A., and Honig, B. (1994) Accurate calculation of hydration free energies using macroscopic solvent models. *J. Phys. Chem. 98*, 1978–1988.
18. Cheatham, T. E., Cieplak, P., and Kollman, P. A. (1999) A modified version of the Cornell et al. force field with improved sugar pucker phases and helical repeat. *J. Biomol. Struct. Dyn. 16*, 845–862.
19. Koerner, J. B., and Ichiye, T. (1997) Conformational dependence of the electronic properties of $[Fe(SCH_3)_4]^{-,2-}$. *J. Phys. Chem. B 101*, 3633–3643.
20. Beck, B. W., Koerner, J. B., and Ichiye, T. (1999) Ab initio quantum mechanical study of metal substitution in analogues of rubredoxin: Implications for redox potential control. *J. Phys. Chem. B 103*, 8006–8015.
21. Sakharov, D. V., and Lim, C. (2005) Zn Protein Simulations Including Charge Transfer and Local Polarization Effects. *J. Am. Chem. Soc. 127*, 4921–4929.
22. Eidsness, M. K., Richie, K. A., Burden, A. E., Kurtz, D. M., and Scott, R. A. (1997) Dissecting contributions to the thermostability of *Pyrococcus furiosus* rubredoxin: β-Sheet chimeras. *Biochemistry 36*, 10406–10413.
23. Eigen, M. (1964) Proton transfer, acid-base catalysis, and enzymatic hydrolysis. (I) Elementary processes. *Angew. Chem., Int. Ed. 3*, 1–19.

24. Molday, R. S., and Kallen, R. G. (1972) Substituent Effects on Amide Hydrogen Exchange Rates in Aqueous Solution. *J. Am. Chem. Soc. 94*, 6739–6745.
25. Kim, P. S., and Baldwin, R. L. (1982) Influence of Charge on the Rate of Amide Proton Exchange. *Biochemistry 21*, 1–5.
26. Delepierre, M., Dobson, C. M., Karplus, M., Poulsen, F. M., States, D. J., and Wedin, R. E. (1987) Electrostatic Effects and Hydrogen Exchange Behavior in Proteins. The pH Dependence of Exchange Rates in Lysozyme. *J. Mol. Biol. 197*, 111–122.
27. Perrin, C. L., Chen, J. H., and Ohta, B. K. (1999) Amide Proton Exchange in Micelles. *J. Am. Chem. Soc. 121*, 2448–2455.
28. Bai, Y. W., Milne, J. S., Mayne, L., and Englander, S. W. (1993) Primary structure effects on peptide group hydrogen-exchange. *Proteins: Struct., Funct., Genet. 17*, 75–86.
29. Avbelj, F., and Baldwin, R. L. (2004) Origin of the neighboring residue effect on peptide backbone conformation. *Proc. Natl. Acad. Sci. U.S.A. 101*, 10967–10972.
30. Fogolari, F., Esposito, G., Viglino, P., Briggs, J. M., and McCammon, J. A. (1998) pKa Shift Effects on Backbone Amide Base-Catalyzed Hydrogen Exchange Rates in Peptides. *J. Am. Chem. Soc. 120*, 3735–3738.
31. Hernández, G., Anderson, J. S., and LeMaster, D. M. (2008) Electrostatic stabilization and general base catalysis in the active site of the human protein disulfide isomerase **a** domain monitored by hydrogen exchange. *ChemBioChem 9*, 768–778.
32. Sharp, K. A., and Honig, B. (1990) Electrostatic Interactions in Macromolecules: Theory and Applications. *Annu. Rev. Biophys. Biophys. Chem. 19*, 301–332.
33. LeMaster, D. M., Anderson, J. S., Wang, L., Guo, Y., Li, H., and Hernández, G. (2007) NMR and X-ray analysis of structural additivity in metal binding site-swapped hybrids of rubredoxin. *BMC Struct. Biol. 7*, 81.
34. Strop, P., and Mayo, S. L. (2000) Contribution of surface salt bridges to protein stability. *Biochemistry 39*, 1251–1255.
35. LeMaster, D. M., and Hernández, G. (2005) Additivity in both Thermodynamic Stability and Thermal Transition Temperature for Rubredoxin Chimeras via Hybrid Native Partitioning. *Structure 13*, 1153–1163.
36. LeMaster, D. M., Anderson, J. S., and Hernández, G. (2006) Role of Native-State Structure in Rubredoxin Native-State Hydrogen Exchange. *Biochemistry 45*, 9956–9963.
37. Anderson, J. S., LeMaster, D. M., and Hernández, G. (2006) Electrostatic Potential Energy within a Protein Monitored by Metal Charge-Dependent Hydrogen Exchange. *Biophys. J. 91*, L93–L95.
38. LeMaster, D. M., Anderson, J. S., and Hernández, G. (2007) Spatial distribution of dielectric shielding in the interior of *Pyrococcus furiosus* rubredoxin as sampled in the subnanosecond timeframe by hydrogen exchange. *Biophys. Chem. 129*, 43–48.
39. LeMaster, D. M., Minnich, M., Parsons, P. J., Anderson, J. S., and Hernández, G. (2006) Tetrathiolate coordination of germanium(IV) in a protein active site. *J. Inorg. Biochem. 100*, 1410–1412.
40. Demchuk, E., and Wade, R. C. (1996) Improving the continuum dielectric approach to calculating pKa's of ionizable groups in proteins. *J. Phys. Chem. 100*, 17373–17387.
41. Schutz, C. N., and Warshel, A. (2001) What are the dielectric "constants" of proteins and how to validate electrostatic models. *Proteins: Struct., Funct., Genet. 44*, 400–417.
42. Li, H., Robertson, A. D., and Jensen, J. H. (2005) Very fast empirical prediction and rationalization of protein pKa values. *Proteins: Struct., Funct., Bioinf. 61*, 704–721.
43. Garcia-Moreno, B., Dwyer, J. J., Gittis, A. G., Lattman, E. E., Spencer, D. S., and Stites, W. E. (1997) Experimental Measurement of the Effective Dielectric in the Hydrophobic Core of a Protein. *Biophys. Chem. 64*, 211–224.
44. Alexov, E. G., and Gunner, M. R. (1999) Calculated Protein and Proton Motions Coupled to Electron Transfer: Electron Transfer from Q_A^- to Q_B in Bacterial Photosynthetic Reaction Centers. *Biochemistry 38*, 8253–8270.
45. Dwyer, J. J., Gittis, A. G., Karp, D. A., Lattman, E. E., Spencer, D. S., Stites, W. E., and Garcia-Moreno, E. B. (2000) High apparent dielectric constants in the interior of a protein reflect water penetration. *Biophys. J. 79*, 1610–1620.
46. Kato, M., and Warshel, A. (2006) Using a charging coordinate in studies of ionization induced partial unfolding. *J. Phys. Chem. B 110*, 11566–11570.
47. Ellison, W. J., Lamkaouchi, K., and Moreau, J. M. (1996) Water: A dielectric reference. *J. Mol. Liq. 68*, 171–279.
48. LeMaster, D. M. (1999) NMR Relaxation Order Parameter Analysis of the Dynamics of Protein Sidechains. *J. Am. Chem. Soc. 121*, 1726–1742.
49. Skrynnikov, N. R., Millet, O., and Kay, L. E. (2002) Deuterium Spin Probes of Side-Chain Dynamics in Proteins. 2. Spectral Density Mapping and Identification of Nanosecond Time-Scale Side-Chain Motions. *J. Am. Chem. Soc. 124*, 6449–6460.
50. Ponder, J. W., and Case, D. A. (2003) Force fields for protein simulations. *Adv. Protein Chem. 66*, 27–85.
51. Friesner, R. A. (2006) Modeling polarization in proteins and protein-ligand complexes: Methods and preliminary results. *Adv. Protein Chem. 72*, 79–104.
52. Feig, M., Onufriev, A., Lee, M. S., Im, W., Case, D. A., and Brooks, C. L. (2004) Performance comparison of generalized Born and Poisson methods in the calculation of electrostatic solvation energies for protein structures. *J. Comput. Chem. 25*, 265–284.
53. Onufriev, A., Bashford, D., and Case, D. A. (2004) Exploring protein native states and large-scale conformational changes with a modified generalized Born model. *Proteins 55*, 383–394.
54. Day, M. W., Hsu, B. T., Joshua-Tor, L., Park, J. B., Zhou, Z. H., Adams, M. W. W., and Rees, D. C. (1992) X-ray crystal structures of the oxidized and reduced forms of the rubredoxin from the marine hyperthermophilic archaebacterium *Pyrococcus furiosus*. *Protein Sci. 1*, 1494–1507.
55. Wolfenden, R. (2003) Thermodynamic and extrathermodynamic requirements of enzyme catalysis. *Biophys. Chem. 10*, 559–572.

BI800284Y